

# Breaking the degeneracy of cosmological parameters in galaxy redshift surveys

Mikel Susperregi

*Fisika Teorikoaren Saila, Zientzi Fakultatea, Euskal Herriko Unibertsitatea, PO Box 644, 48080 Bilbao, Spain*  
*Email: wtpsuxm@ehu.es*

27 October 2018

## ABSTRACT

The measurement of cosmological parameters is investigated in a representation of the least-action method that uses a redshift-space dataset to simultaneously constrain the real-space fields  $\delta, \vec{v}$ . This method is robust in recovering the entire evolution of the matter density contrast and peculiar velocities of galaxies in real space from current galaxy redshift surveys. The main strength of the method is that it permits us to break the degeneracy of the parameters  $b$  and  $\Omega_m$  (customarily measured in the ratio  $\beta \equiv \Omega_m^{0.6}/b$  from redshift-space distortions), and these are evaluated in the current context separately. The procedure provides a simple numerical means to extract as much information as possible from a given sample, in the simplest linear bias model, before resorting to cosmic complementarity to resolve the degeneracy in the measurement of  $\Omega_m$ . The same premise applies to more sophisticated choices of bias models. We construct a likelihood parameter  $\lambda(b, \Omega_m)$  to evaluate the relative likelihood of different values of  $b$  and  $\Omega_m$ . The method is applied to the *IRAS* 1.2 Jy redshift survey with a low-resolution Gaussian smoothing length of  $1200 \text{ km s}^{-1}$  within a spherical region  $x_{\max} \sim 15,000 \text{ km s}^{-1}$  and the reconstructed velocity field is then compared with POTENT-reconstructed velocities from the Mark III radial-velocity dataset within a radius  $\sim 5000 \text{ km s}^{-1}$ , which have been suitably prepared to account for Malmquist bias and other systematic errors. The analysis yields a likelihood for the parameters that is overall consistent with  $\Omega_m \approx 0.3$  and  $b \approx 1.1$ , thus lending support to a non-vanishing cosmological constant  $\Omega_\Lambda \approx 0.7$  in a flat universe.

**Key words:** large-scale structure of universe – cosmology – galaxies: distances and redshifts

## 1 INTRODUCTION

Galaxy redshift surveys are undoubtedly extremely valuable tools to investigate the evolution of the universe at large scales. The cosmologist’s prerogative is to determine the evolution of the matter density contrast  $\delta$  and peculiar velocity  $\vec{v}$  that yields such cosmic structure, customarily assuming that it formed solely by gravity, and the cosmological parameters that determine their dynamics. In the standard paradigm of a FRW expanding universe, the interplay of both fields is governed by the density parameter  $\Omega_0$  and the Hubble parameter  $H_0$ . On the other hand, a relationship between the fields  $\delta, \vec{v}$  and the survey data is established by adopting a bias model that purports the correlation between the  $z$ -space galaxy number-count and the underlying matter field. Devoid of such a relationship, the edifice of measuring cosmological parameters from galaxy redshift surveys has no foundation whatsoever. A standard working hypothesis, that I shall accept throughout this paper, is that of linear bias, i.e.  $b^2 \equiv P(k)_{\text{gals}}/P(k)_{\text{matter}}$  (more elaborate bias models

are propounded in e.g. Dekel & Lahav 1999). For simplicity we shall also leave out the scale-dependence of  $b$ . Therefore, three relevant parameters that are interesting to pin down from redshift-space samples are in this context  $\Omega_m, H_0$  and  $b$ . In this paper I shall be chiefly concerned with  $\Omega_m$  and  $b$  ( $H_0$  will be scaled out with distance).

Tracing back in time the matter fields takes us to an initial epoch of fluctuations of very small amplitude  $\delta \lesssim 10^{-4}$ , seeded by a period of inflationary expansion. At that point the information derived from the galaxy surveys connects with early-universe data such as the spectrum of fluctuations on the CMB. If the matter fields could realistically be traced back to such a primordial stage by integrating the equations of gravitational instability, then the statistics of the  $\delta$  field would be a potentially key discriminant to rule out cosmological models. For instance, non-gaussianity in the initial  $\delta$  field rules out most inflationary models, and only those leading to a non-Gaussian primordial spectrum

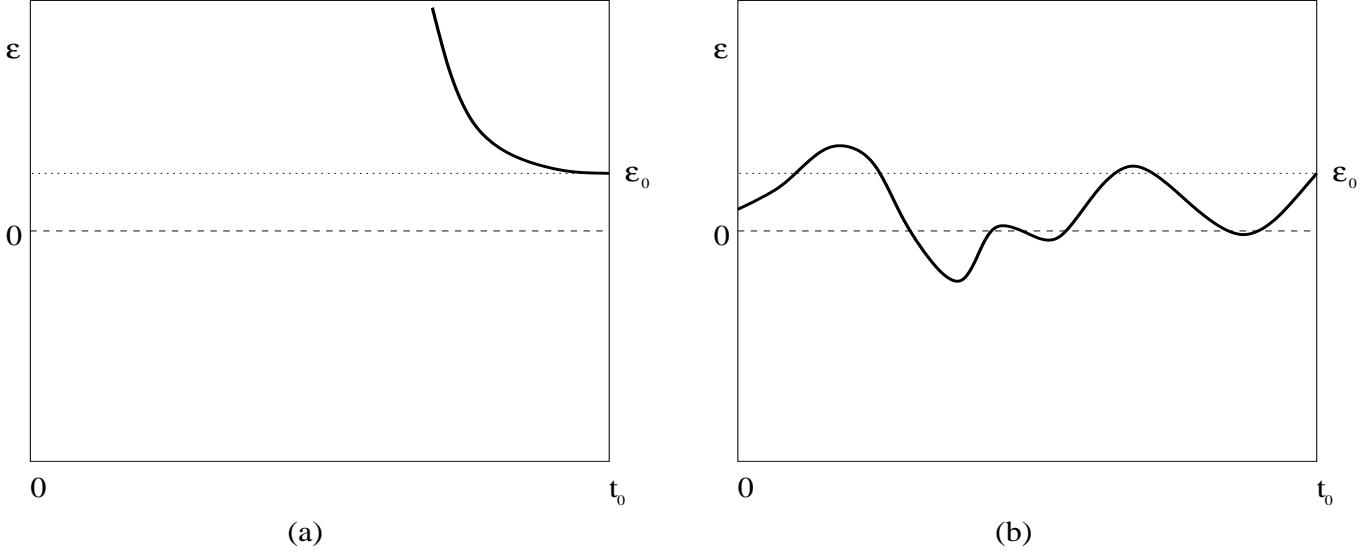


**Figure 1.** Qualitative distribution of errors in the reconstruction of the matter fields from redshift surveys. The error  $\epsilon_0$  in the current redshift sample increases monotonically in (a) as the perturbative solutions propagate  $\epsilon_0$  to increasing amplitudes when integrated back in time; in the boundary condition problem of the LAP method, shown in (b), errors fluctuate between the fixed end-points.

remain acceptable (such models are suggested in e.g. Linde, Sasaki & Tanaka 1999).

Kaiser (1987) proposed measuring cosmological parameters from redshift-space distortions by virtue of the fact that overdense regions appear to be flatter along the line-of-sight in redshift space. This distortion, quantified by the parameter  $\beta = \Omega_m^{0.6}/b$ , permits us to solve the equations for  $\delta, \vec{v}$ , at least perturbatively (see e.g. Dekel 1994; Coles & Sahni 1995), and measurements of  $\beta$  have been investigated in much detail in the literature (Strauss & Willick 1995; Dekel 1994, 1999a; Dekel, Burstein & White 1997). Also, in view of the fact that the bias parameter is almost certainly dependent on the selected sample, estimates have been computed for  $\beta_{IRAS}$  given  $b_I$  for *IRAS* galaxies (Dekel *et al.* 1993; Fisher *et al.* 1995a; Willick *et al.* 1997a,b; Sigad *et al.* 1998; more recently from the PSCz sample, Canaverez *et al.* 1998; Tadros *et al.* 1999; Saunders *et al.* 2000) and from the Optical Redshift Survey (ORS) (Hudson *et al.* 1995; Santiago *et al.* 1995; Baker *et al.* 1998). The Mark III peculiar velocity survey similarly yields estimates of  $\beta$  from redshift distortions (Willick *et al.* 1995, 1996, 1997a,b; Dekel, Burstein & White 1997; Sigad *et al.* 1998). It is only beyond the linear approximation (i.e.  $\delta \propto \nabla \cdot \vec{v}$ ) and, indeed, beyond the assumption of linear bias, that one can break down the degeneracy between  $\Omega_m$  and  $b$  and estimate these parameters separately, rather than via  $\beta$  (Fry 1994; Bernardreau *et al.* 1995). Verde *et al.* (1998) achieved this by proposing the bispectrum as a measure of cosmological parameters, in a model of non-linear bias. In this paper we also pursue breaking the degeneracy of  $\Omega_m$  and  $b$  from the redshift-space data and show that by using the least-action framework it is indeed possible to do so within the linear bias model.

The least-action principle (LAP) was first used in the Local Group by Peebles (1989, 1990). The trajectories of nearby galaxies were computed subject to two boundary conditions: vanishing initial velocities and fixed present positions. This simple scenario of self-gravitating point-like

masses with two boundary conditions produced an estimate of  $\Omega_m$  by fitting to the observations the predicted peculiar velocities of nearby galaxies. The LAP method has also been used as a test of  $\Omega_m = 1$  CDM models (Branchini & Carlberg 1994), as well as to integrate the orbits of a significant number of galaxies from partial coverage redshift samples (e.g. Shaya, Peebles & Tully 1995). An equivalent representation of the LAP method in terms of continuous fields, i.e. the density contrast and velocity fields was proposed by Giavalisco *et al.* (1993), and employed in Susperregi & Binney (1994) (hereafter SB94) and Susperregi (1995) in the reconstruction of  $\Omega_m = 1$  simple models, such as exact solutions and Gaussian random fields. More recently, Schmoldt & Saha (1998) proposed a variant of the customary LAP formulation by rewriting the equations motion in redshift space.

The key difference between the variational and perturbative approaches lies on how the errors are spread over the time-reversed evolution. This is qualitatively sketched in Fig. 1. A  $n$ th-order solution differs, in the time-reversed direction, from the true solution by a monotonically growing parameter  $\epsilon$  which sets out from a small value  $\epsilon(t_0)$  (at any rate  $\epsilon_0$  is at least the sum of the systematic and random errors of the dataset) and the conservation of kinematical quantities is preserved up to  $O(\epsilon^n)$ . This is adequate within a time span  $t_c \ll t \lesssim t_0$  where  $\epsilon(t_c) \sim 1$ , and  $t_c$  marks a transition into the loss of convergence. The distribution of errors in the LAP method on the other hand, is by construction evenly distributed along the trajectory; the initial and final boundary conditions are fixed, though not without systematic and numerical errors, and the parameter  $\epsilon$  fluctuates along the trajectory between both end-points (Fig. 1b). Hence the solution is well-behaved whether the errors remain within the bound  $\epsilon \lesssim 1$  or not. In that respect there is an advantage with respect to perturbative solutions; the downside of it is of course that within the span of time where perturbative solutions are valid, LAP errors may fluctuate

with larger amplitude than the perturbative equivalent. The LAP method, in a nutshell, thus consists in finding Ansätze for the matter fields that optimize the distribution of  $\epsilon$  along the phase-space trajectory, and hence minimize the overall departure with respect to the exact solution. The following two difficulties may arise:

- **A** *Finding “dynamically plausible” solutions.* If the matter field is sparsely sampled or the errors in the dataset are substantial, then the boundary condition given by the survey, taken at face value, may not correspond to the outcome of gravitational evolution from the initial fluctuations (typically  $\delta \sim 0$  or vanishing peculiar velocities). The LAP method will in this case find a *dynamically plausible* fit between the end-points, which will be as faithful a representation of the true evolution as is the quality of the dataset.

- **B** *Formation of multistreams in over-dense regions.* Multistreams are characterised by galaxies at the same redshift which are located at different positions along the line of sight and have different infalling velocities. The degeneracy in redshift among streams makes them indistinguishable and hence compatible but inequivalent solutions result, as many as there are streams. The LAP method cannot discriminate among these solutions; multistreams indeed erase the memory of their past evolution.

The second problem can only be overcome by casting aside part of the information contained in the sample and smoothing over the existing non-linearities to transform the multi-valued field into a single-valued one, typically with a smoothing length  $\sim 500 - 1000 \text{ km s}^{-1}$ . The resulting smoothed field is clearly a less resolved representation of the underlying galaxy orbits, albeit the only tractable one.

The advent of large galaxy redshift surveys strengthens the motivation to use the LAP method. Near all-sky redshift surveys, e.g. PSCz, *IRAS* 1.2 Jy and ORS provide an excellent sky coverage (within a galactic latitude  $|b| \gtrsim 8^\circ$  for *IRAS* galaxies and  $|b| \gtrsim 20^\circ$  for ORS), that may be extended further to cover the Zone of Avoidance via a Wiener reconstruction (Fisher *et al.* 1995b; Zaroubi *et al.* 1999). They are therefore a fairly thorough representation of the underlying matter density field. Obviously the greater number of galaxies in the sample the more accurate is the representation of the field, and this is best achieved with a redshift survey. Real-space datasets require Tully-Fisher distance calibrations of individual galaxies, and consequently the end result is a sparser sampling than is achieved with the same computational effort by measuring redshifts and angular coordinates. The goal of this paper is to exploit galaxy redshift surveys to the best effect and extract as much information from them as is possible; the main thesis put forward is the LAP method demonstrably breaks down the degeneracy in the determination of  $\Omega_m$  and  $b$ . This entails very tangible advantages. On the one hand, the freedom to investigate those two parameters separately permits us not to take the idea of bias seriously. A form of bias will certainly always be present in one form or another so that we can make sense of the galaxy number-count with respect to the underlying matter field. However, whether that is a linear or non-linear bias, the more one dissociates this phenomenological relationship from our measurements of  $\Omega_m$ , the more credible those measurements will be. This is indeed what LAP does. On the other hand, the LAP method produces a reconstruc-

tion on the basis of the redshift-space sample alone, free of any proviso regarding the shape of the power spectrum. Assuming a given shape for  $P(k)$  unduly overconstrains the system, as will the addition of other datasets.

In this article, I shall mainly apply the LAP method to the *IRAS* 1.2 Jy survey and study the predicted values of  $b$  and  $\Omega_m$ . The reconstructed *IRAS* 1.2 Jy velocity field is then compared with the Mark III velocity sample to seek a fine-tuning of the parameters. A more thorough undertaking, in terms of the quality of the sample, is to apply the LAP method to PSCz, which is by a factor of 3 a more densely sampled survey than *IRAS* 1.2 Jy, and it will be interesting to tackle this in future work. The article is structured as follows: Section 2 describes the LAP method in some detail and how to find solutions that are consistent with a redshift-space dataset; in Section 3 we test the method with several *IRAS* mock catalogues obtained via *n*-body simulations; in Section 4 we apply the method to the *IRAS* 1.2 Jy galaxy redshift survey, optimizing the predicted velocities with the Mark III dataset; finally, in Section 5 we summarize the main conclusions.

## 2 THE LAP METHOD

### 2.1 Redshift-space coordinates

The redshift coordinates of galaxies are defined

$$\vec{z} = H_0 \vec{r} + \hat{r}(\hat{r} \cdot \vec{v}), \quad (1)$$

where  $\vec{r} \equiv (r, \theta, \varphi)$  is the physical position,  $H_0$  is the present value of the Hubble parameter,  $\vec{v}$  the peculiar velocity, and  $\hat{r}$  a unit vector in the radial (line-of-sight) direction.  $\vec{z}$  has units of velocity; its radial component is the redshift  $z_r = cz$ , and the angular components are the same in both  $x$ -space and  $z$ -space, up to the distance scale. Henceforth we shall measure distances in  $\text{km s}^{-1}$ , hence  $H_0$  is scaled out of the equations. In comoving coordinates, (1) reads

$$\vec{s} = \vec{x} + \hat{x}(\hat{x} \cdot \nabla_x \alpha), \quad (2)$$

where the scale factor of the universe is normalized to  $a(t_0) = 1$ ;  $\alpha(t, \vec{x})$  is the velocity potential,  $\vec{v} \equiv a^{-1} \nabla \alpha$ . Hereafter we adopt  $t_0 = 1$ .

### 2.2 Dynamics

The cosmological perturbations are derived from the action

$$\mathcal{S} = \int_0^1 dt \int_{\text{sample}} d\vec{x} \mathcal{L}, \quad (3)$$

where  $\mathcal{L}$  is given by

$$\mathcal{L} = \frac{1}{2} (1 + \delta) \vec{v}^2 + \alpha \xi - \phi \delta - \frac{|\nabla \phi|^2}{3 \Omega_m a^2}; \quad (4)$$

$\delta$  is the density contrast and  $\phi$  the gravitational potential caused by the perturbations and

$$\xi \equiv \dot{\delta} + \frac{1}{a} \nabla \cdot [(1 + \delta) \vec{v}] \quad (5)$$

is the *excess flux*. The variations  $\delta \mathcal{S} / \delta v_i = \delta \mathcal{S} / \delta \phi = 0$  yield

$$\vec{v} = \frac{1}{a} \nabla \alpha, \quad (6)$$

$$\nabla^2 \phi = \frac{3}{2} a^2 \Omega_m \delta. \quad (7)$$

Similarly,  $\delta S/\delta\delta = \delta S/\delta\alpha = 0$  yield respectively

$$\xi = 0, \quad (8)$$

$$\dot{\alpha} + \frac{|\nabla\alpha|^2}{2a^2} + \phi = 0, \quad (9)$$

where we have eliminated  $\vec{v}$  via (6) and we do not consider  $\Omega_\Lambda$ . The field equations (8),(9) are subject to the following boundary conditions:

I *Homogeneity of the density field at  $t \rightarrow 0$* . Density perturbations grow from initial fluctuations of negligible amplitude:

$$\delta(t \rightarrow 0, \vec{x}) \approx 0. \quad (10)$$

II *Galaxy redshift survey at the present time*. The galaxy number-count density  $\rho_s$  in  $z$ -space constrains the real fields  $\delta(\vec{x})$  and  $\alpha(\vec{x})$  via

$$\rho_s(\vec{s}) = x^2 \frac{N_{\text{gals}}}{V} \left( \frac{1 + b\delta}{1 + \alpha''} \right), \quad (11)$$

where the tilde denotes derivation along the radial direction,  $x$  is the radial comoving distance and  $b$  is the bias parameter. Condition (I) is motivated by the CMB Sachs-Wolfe constraint  $\delta \lesssim 10^{-4}$  over  $r \sim 100,000 \text{ km s}^{-1}$ , so we accept that perturbations are negligible in the limit  $t \rightarrow 0$ . A proof for (II) is given in Appendix A. In order to solve (8),(9), we construct the trial fields:

$$\delta = \sum_{n=0}^N f_n(t) \delta_n(\vec{x}), \quad (12)$$

$$\alpha = \sum_{n=0}^N g_n(t) \alpha_n(\vec{x}), \quad (13)$$

where the basis functions  $f_n, g_n$  are adjusted to numerical convenience. SB94 considered  $f_n \equiv D(D-1)^n$ , and  $g_n = (\dot{D}/D)f_n$ , where  $D$  is the linear growth factor, normalized to unity at  $t = 1$ , so that the lowest-order series (12),(13) are identical to the perturbative solutions. This is however strictly speaking not a compelling choice, and a sensible choice of orthogonal polynomials leads to an Ansatz of better convergence. As we have discussed in the Introduction (point A), the sparseness of the dataset obscures the dynamical evolution and the LAP method is reduced to a numerical fit of the fields to the truncated equations, that we derive below, subject to (10),(11). In trying to approximate a function  $f(t)$  by orthogonal polynomials  $P_m(t)$  in  $0 \lesssim t \lesssim 1$ , a weight function  $w(t) \geq 0$  tells us the relative importance of the errors spread over the domain. For a uniform  $w$ ,  $f_n$  are the [spherical] Legendre polynomials  $L_m(t)$ , whereas for a weight function that is larger at the endpoints (10),(11) than throughout the trajectory, e.g.  $w(t) = (1-t^2)^{-1/2}$  (by shifting the domain from  $[0, 1]$  to  $[-1, 1]$ ), the optimal choice are in this case Chebyshev polynomials  $T_n(t)$ . This choice minimizes the errors around the endpoints and it gives a greater weight to the solutions (matching the boundary conditions) in this region. In the analysis that follows, we shall adopt  $f_n = T_n$  and  $g_n = a^2 f_n$ . The fields  $\delta_n, \alpha_n$  are expanded in terms of spherical harmonics,

$$\delta_n = \sum_{rlm} \delta_{rlm}^{(n)} j_l(k_r x) Y_{lm}, \quad (14)$$

$$\alpha_n = \sum_{rlm} \alpha_{rlm}^{(n)} j_l(k_r x) Y_{lm}, \quad (15)$$

where  $j_l$  are spherical Bessel functions. Substituting (12),(13) into (6),(7) we get

$$\vec{v} = a \sum_{rlmn} \left[ \hat{x} \alpha'_{rlm}^{(n)} j_l(k_r x) + \frac{1}{x} (\hat{x} \wedge \vec{J}_{lm}^{(n)}) \right] T_n Y_{lm}, \quad (16)$$

$$\phi = -\frac{3}{2} a^2 \Omega_m \sum_{rlmn} \frac{\delta_{rlm}^{(n)}}{k_r^2} T_n j_l(k_r x) Y_{lm}; \quad (17)$$

the coefficients  $\alpha'_{rlm}^{(n)}$  and  $\vec{J}_{lm}^{(n)}$  are given in Appendix B. The boundary conditions (10),(11) then read

$$0 = \sum_{n=0}^N (-1)^n \delta_n, \quad (18)$$

$$\rho_s = x^2 \left( \frac{N_{\text{gals}}}{V} \right) \left[ 1 + b \delta(1, \vec{x}) \right] \left[ 1 + \alpha''(1, \vec{x}) \right]^{-1}, \quad (19)$$

where  $t$  is rescaled to the interval  $[-1, 1]$  for convenience in using  $T_n$ , and in (18) we have used  $T_n(-1) = (-1)^n$ . The choice of basis functions of SB94 satisfy (18) by construction, and in our choice of basis functions the constraint is less trivial, but still it is easily tackled numerically. If we restrict ourselves to the interval  $0 \leq t \leq 1$ , then (18) evaluated at  $t = 0$  eliminates all the Chebyshev polynomials of odd order. This is an equivalent approach but we shall adopt the convention above,  $-1 \leq t \leq 1$ . The constraint (19) is the core of the problem as it is where all the information of the dataset is contained. The remainder of the paper will focus on the different ways one can use that constraint.

### 2.3 Finding LAP solutions

Substituting (12)–(15) into equations (8),(9), we get

$$\begin{aligned} & \sum_{n=0}^N \sum_{rlm} \left[ \dot{T}_n \delta_{rlm}^{(n)} - k_r^2 T_n \alpha_{rlm}^{(n)} \right] j_l(k_r x) Y_{lm} \\ &= - \sum_{p,q=0}^N \sum_{\substack{r'l'm' \\ r'l'm'}} T_p T_q \left\{ \alpha'_{rlm}^{(q)} \delta'_{r'l'm'}^{(p)} j_l(k_r x) j_{l'}(k_{r'} x) \right. \\ & \quad \left. + \frac{1}{x^2} \left[ \hat{x} \wedge \vec{J}_{lm}^{(p)}(\delta) \right] \cdot \left[ \hat{x} \wedge \vec{J}_{l'm'}^{(q)}(\alpha) \right] \right\} Y_{lm} Y_{l'm'}, \end{aligned} \quad (20)$$

and

$$\begin{aligned} & \sum_{n=0}^N \sum_{rlm} \left[ -\frac{3}{2} \Omega_m k_r^{-2} \delta_{rlm}^{(n)} + \left( \frac{\dot{T}_n}{T_n} + 2 \frac{\dot{a}}{a} \right) \alpha_{rlm}^{(n)} \right] T_n j_l(k_r x) Y_{lm} \\ &= -\frac{1}{2} \sum_{p,q=0}^N \sum_{\substack{r'l'm' \\ r'l'm'}} T_p T_q \left\{ \alpha'_{rlm}^{(q)} \alpha'_{r'l'm'}^{(p)} j_l(k_r x) j_{l'}(k_{r'} x) \right. \\ & \quad \left. + \frac{1}{x^2} \left[ \hat{x} \wedge \vec{J}_{lm}^{(p)}(\alpha) \right] \cdot \left[ \hat{x} \wedge \vec{J}_{l'm'}^{(q)}(\alpha) \right] \right\} Y_{lm} Y_{l'm'}, \end{aligned} \quad (21)$$

where the coefficients  $\tilde{J}_{lm}^{(p)}(\delta), \tilde{J}_{lm}^{(q)}(\alpha)$  are defined as in (B5) in Appendix B and  $\delta'_{rlm}$  as in (B3) via the trivial substitution  $\alpha \rightarrow \delta$ . By multiplying (20),(21) by  $T_{rl} Y_{lm}$  and integrating over all coordinates, we get

$$\begin{aligned} & \sum_{n=0}^N \langle T_r \dot{T}_n \rangle C_y^\delta \delta_y^{(n)} + \sum_{n=0}^N \langle T_r T_n \rangle C_y^\alpha \alpha_y^{(n)} \\ &= - \sum_{p,q=0}^N \langle T_r T_p T_q \rangle \sum_{y'y''} D_{y'y''}^y \delta_{y'}^{(p)} \alpha_{y''}^{(q)}, \end{aligned} \quad (22)$$

$$\begin{aligned} & \sum_{n=0}^N \Omega_m \langle T_r T_n \rangle S_y^\delta \delta_y^{(n)} + \sum_{n=0}^N \langle T_r (\dot{T}_n + 2 \frac{\dot{a}}{a} T_n) \rangle S_y^\alpha \alpha_y^{(n)} \\ &= - \sum_{p,q=0}^N \langle T_r T_p T_q \rangle \sum_{y'y''} E_{y'y''}^y \alpha_{y'}^{(p)} \alpha_{y''}^{(q)}, \end{aligned} \quad (23)$$

where  $y \equiv (rlm)$  and the angle brackets  $\langle \rangle$  for the Chebyshev polynomials are defined in Appendix C. In deriving (22),(23), the coefficients  $C_y^\delta, C_y^\alpha, S_y^\delta, S_y^\alpha, D_{y'y''}^y$  and  $E_{y'y''}^y$  are calculated via Clebsch-Gordan coefficients for cross-products of  $Y_{lm}$  and via the standard orthogonality relations for  $Y_{lm}$  and  $j_l$ , given in Appendix D. Cross-products of  $j_l$  terms are estimated numerically. We proceed to solve (22),(23) numerically with the following iterative procedure. We first construct an Ansatz of the coefficients  $\delta_y^{(n)}, \alpha_y^{(n)}$  that satisfies, to linear order, (22),(23) as well as (18),(19). We start out with the galaxy number-count density  $\rho_s$ . Following its definition in Appendix A, this quantity has units of inverse velocity, and we define its associated  $z$ -space density contrast via

$$\rho_s \equiv \frac{4\pi N_{\text{gals}}}{s_{\text{max}}} (1 + \delta_s), \quad (24)$$

where  $s_{\text{max}} \equiv cz_{\text{max}}$  is the maximum redshift in the sample. Our first Ansatz entails  $b = 1$  and linear evolution, so that  $\delta_s \propto -\nabla^2 \alpha$ , and on inverting this relation to obtain the coefficients  $\alpha_y^{(n)}$ , we estimate  $\delta(\vec{x}) \propto \delta_s(\vec{x} + \hat{x}\alpha')$  by using the expression for the radial derivatives (B3). This yields a first Ansatz for  $\delta_y^{(n)}, \alpha_y^{(n)}$ , derived from the dataset, that satisfies the linearized equations, given by the LHS of (22),(23):

$$\begin{bmatrix} C^\alpha & C^\delta \\ S^\alpha & S^\delta \end{bmatrix} \begin{bmatrix} \vec{\alpha}_y \\ \vec{\delta}_y \end{bmatrix} \approx 0, \quad (25)$$

where the column vectors are  $(\vec{\alpha}_y)_r = \alpha_y^{(r)}$  and  $(\vec{\delta}_y)_r = \delta_y^{(r)}$ , with  $r = 0, \dots, N$ . The solutions of the homogeneous system are then re-adjusted to satisfy (18),(19) and we use these to construct the quadratic terms on the RHS of (22),(23). This leads to an inhomogeneous system that again we solve for  $\vec{\delta}_y, \vec{\alpha}_y$ . On each iteration we improve the solutions by least-squaring them to satisfy (18),(19) to the best accuracy and we are also free to vary the parameters  $(b, \Omega_m)$  for improved convergence. This procedure is very accurate, as we will show in the next sections, and it permits us to improve the estimate of the mapping  $\vec{x} \rightarrow \vec{s}$  at each iteration using the full non-linear relationship (19). At each iteration, the fields  $\vec{\delta}_y, \vec{\alpha}_y$  are used to obtain an estimate  $\tilde{\rho}_s(\vec{s})$  of the RHS of (19). We then vary these fields to obtain a minimum of the quantity  $\sum_{\vec{s}} (\rho_s - \tilde{\rho}_s)^2$ . Therefore we do not perform a  $j_l Y_{lm}$  expansion of the dataset, and it is very convenient not

to do so, as a relationship of this kind between the redshift and real-space coordinates entails that we compare them via a Taylor expansion  $j_l(k_r s) \approx j_l(k_r x) + k_r \alpha' j_l'$ ; an approximation of this kind  $\sim \mathcal{O}(\partial^2 j_l)$  introduces an error of up to 15% for  $l \gtrsim 10$  as can be shown from (B2) in Appendix B.

## 2.4 Normal modes

We have noted that the linearized equations (25) are a homogeneous matrix system. If the determinant of the matrix is non-zero, then the only possible solution is  $\vec{\delta}_y = 0$  and  $\vec{\alpha}_y = 0$ . We know however that (25) is also valid for linear fields, and these have non-vanishing coefficients. Therefore we conclude that the determinant of the system vanishes. Such a system of equations is tackled through the Singular Value Decomposition (SVD) procedure. It factorises the singular matrix in (25) in a product of three matrices: two orthogonal matrices  $U$  and  $V$ , and a diagonal one  $W$ , which has one or more vanishing *weights* along the diagonal. After SVD, (25) reads

$$U \begin{bmatrix} 0 & & & \\ & w_1 & & \\ & & w_2 & \\ & & & \ddots \end{bmatrix} V \begin{bmatrix} \vec{\alpha}_y \\ \vec{\delta}_y \end{bmatrix} = 0, \quad (26)$$

where the weights  $w_1, w_2, \dots, w_N$  are non-zero real numbers. Therefore, the vector

$$\vec{N}_y = V \begin{bmatrix} \vec{\alpha}_y \\ \vec{\delta}_y \end{bmatrix} \quad (27)$$

gives a coordinate basis on which the first component, the *normal mode*, is unconstrained by the system (25).  $N_y^{(0)}$  is solely determined by (18),(19). The rest of the components of  $\vec{N}_y$  (which are identically zero for linear fields) are functions of the normal mode. Therefore, one can rewrite the full non-linear system (22),(23) in terms of the fields  $\vec{N}_y$  and this would be strictly speaking the natural basis to investigate the underlying mode coupling induced by gravity. In the Fourier formulation with a set of basis functions like those used in SB94,  $f_n = D(D-1)^n$ , it is easy to show numerically that the  $\vec{k}$ -th normal mode is given by

$$N_{\vec{k}}^{(0)} = \delta_{\vec{k}}^{(0)} + k^2 \alpha_{\vec{k}}^{(0)}. \quad (28)$$

This has a simple physical interpretation: (28) is a vanishing scalar for linear fields and thus its departure from zero gives us a measure of non-linearity. This quantity is determined by the boundary conditions. In the spherical harmonic formulation, the normal modes (equivalent to (28)) are

$$N_y^{(0)} = \sum_{n=0}^N h_n (\delta_y^{(n)} - k_r^{-2} \alpha_y^{(n)}), \quad (29)$$

where

$$h_n = \frac{\eta}{\pi} \int_0^1 dt w(t) D(t) T_n \quad (30)$$

where  $\eta = 1$  for  $n = 0$  and  $\eta = 2$  otherwise. The quantity (29) vanishes in the linear regime and, like (28), its departure from zero is a measure of non-linearity.

## 2.5 Using the method in practice

The apparent mathematical complexity of the LAP method has precluded its wider use in practice. The fraction of papers in the literature that employ LAP techniques to investigate large-scale structure is minute in contrast to analyses based on perturbation theory techniques, such as POTENT, VELMOD and others. The latter unquestionably have the virtue of simplicity, and are as efficient as they are easy to implement. However, in practice the method described in this section entails no more complexity than programming an  $n$ -body code; an undertaking that merits the effort, so as to estimate  $b$  and  $\Omega_m$ , rather than merely  $\beta$ . The chief difficulty resides in writing an algorithm for an effective numerical resolution of (22),(23). This may be a somewhat arduous task, but at any rate a very straightforward one with a very basic grasp of numerical methods.

The LAP method is very flexible in its implementation. The basic input in the problem are the boundary conditions (10), (11) and the procedure that is to be followed to find a stationary action linking both end-points is largely a matter of numerical convenience. The algorithm used in this section employs Chebyshev polynomials to fit the trial fields  $\delta$  and  $\alpha$  to the dynamics. A myriad of other choices (e.g. binomial expansions, Legendre and Hermite polynomials, etc) is also feasible and thus the LAP implementation set out above is by no means a straightjacket recipe (for a more condensed presentation of the algorithm, see Susperregi 2000).

In short, the algorithm can be summarized as follows.

- A galaxy redshift survey is a dataset  $\mathcal{D}$  of points  $(z, \varphi, \theta)$ . Those raw data are transformed to a smoothed redshift-space field  $\rho_s(\vec{s})$ , given a smoothing length and a window function  $W(k)$ . In this article we shall exclusively implement Gaussian smoothing.

- The name of the game is to compute a fit for  $\delta, \alpha$ . The starting point is to make a linear Ansatz that is consistent with  $\delta_s$ , which is derived from (24). This is achieved by inverting the relation  $\delta_s \propto -\nabla^2 \alpha$  and next estimating  $\delta \propto \delta_s(\vec{x} + \hat{x}\alpha')$ .

- The linear Ansatz is the first input to be used in equations (22),(23). These yield the homogeneous system (25), which is our second port of call. The solutions  $\delta_y, \alpha_y$  obtained are least-square fitted to (18),(19). This requires adopting a value of  $b$ .

- The adjusted values of  $\delta_y, \alpha_y$  are brought back to construct the RHS of (22),(23), and from there one computes the new  $\delta_y, \alpha_y$  in the LHS of (22),(23). This part of the operation entails an assumed value for  $\Omega_m$ . In the normal mode coordinates discussed in 2.4, the modes  $\delta_y, \alpha_y$  of the cosmic fields are merely excitation modes of a harmonic oscillator and the terms in the RHS of (22),(23) represent nonlinear perturbations of those excitation modes.

- Successive iterations of the procedure eventually yield the correct values of  $\delta_y, \alpha_y$ . The values of  $b$  and  $\Omega_m$  are readjusted in the process and their estimated values are those that result in the most rapid convergence of the solutions.

The algorithm thus produces the cosmic fields and an estimate of the cosmological parameters. In the remainder of the article we shall investigate how to make the best use of the procedure and how to quantify the relative likelihood of different values of the cosmological parameters.

## 3 TEST OF THE METHOD

We test the LAP method on mock catalogues derived from  $n$ -body simulations, using a Gaussian smoothing length of  $600 \text{ km s}^{-1}$ . The *IRAS* 1.2 Jy power spectrum (Fisher *et al.* 1993) is adopted as a prior, and the simulations are performed over a periodic box  $L = 25,600 \text{ km s}^{-1}$  with  $128^3$  grid-points and  $128^3$  particles. The simulations are performed from Gaussian initial conditions, for the following values of the parameters:  $b = 0.8, 1.0, 1.2$  and  $\Omega_m = 0.3, 0.6, 1.0$ . The fields are evolved forward in time until  $\sigma_8 \approx 0.7$  over  $\sim 800 \text{ km s}^{-1}$ , using a Gaussian cutoff. We choose a two-powerlaw functional form of selection function (Yahil *et al.* 1991):

$$\phi(r \geq r_s) = \left( \frac{r_s}{r} \right)^{2\alpha} \left( \frac{r_*^2 + r_s^2}{r_*^2 + r^2} \right)^\beta, \quad (31)$$

and  $\phi(r \leq r_s) = 1$ , where  $r_s = 500 \text{ km s}^{-1}$ ,  $r_* = 5034 \text{ km s}^{-1}$ ,  $\alpha = 0.483$  and  $\beta = 1.79$  (Fisher *et al.* (1995a); we adopt the estimated central values of these parameters and will not test the fine detail of the variations of  $\phi(r)$  due to their errors), and thus we compute the redshift-space dataset over a sphere of radius  $x_{\max} \sim 17,000 \text{ km s}^{-1}$ . The resulting mock catalogue has an effective radius of  $\sim 13,000 \text{ km s}^{-1}$  beyond which the galaxy number-count is sparse and is cut off for the purpose of the reconstruction. The number of realizations are nine in total, and we denote  $d(b, \Omega_m)$  the  $z$ -space mock samples derived in this way. Each dataset  $d(b, \Omega_m)$  results from a unique pair of real-space fields  $\delta, \alpha$  which are the density contrast and velocity potential that we obtain via the  $n$ -body simulations.

The tests are carried out by using  $d(b, \Omega_m)$  as an input dataset in (19) without any prior assumption on the real values of the parameters of the mock sample. We use (19) to solve (22),(23) following the iterative procedure given in §2.3 and derive the estimated fields  $\tilde{\delta}, \tilde{\alpha}$  for different values of the parameters  $\tilde{b}, \tilde{\Omega}_m$ . The likelihood of these parameters is estimated on the basis of the performance of the solutions  $\tilde{\delta}, \tilde{\alpha}$  in terms of their convergence and ability to satisfy the constraints. We use a likelihood function given by the inverse of the  $\chi^2$ -sum of the differences of the fields between successive iterations in solving (22),(23), i.e.

$$\lambda(b, \Omega_m) \propto \left[ \sum_x \left( \frac{\delta_n - \delta_{n-1}}{\sigma_\delta} \right)^2 + \left( \frac{\alpha_n - \alpha_{n-1}}{\sigma_\alpha} \right)^2 \right]^{-1}, \quad (32)$$

where  $n \geq 25$ ,  $\sigma_\delta \approx 0.20$ ,  $\sigma_\alpha$  is a normalization factor that rescales the coefficients  $\sigma_n$  so that  $\alpha$  becomes a dimensionless field within the range  $-1 \lesssim \alpha \lesssim 1$  and we have used  $N = 10$  and  $l \leq 15$  and an initial linear Ansatz. The results are shown in Fig. 2. The likelihood contours are the LAP reconstructions and the crosses on all nine panels of Fig. 2 indicate the values of the real parameters in each mock dataset on the  $(b, \Omega_m)$  plane. As can be observed, the likelihood contours are certainly well correlated with the location of the crosses, where the innermost contours mark the level of 95% likelihood, that in all cases lie in the neighbourhood of the real values of the parameters. The likelihood contours show an approximately elliptical shape, with the major semiaxes tilted at approximately 45 degrees, suggesting a correlation between both parameters that merely arises in the numerical computation. The estimates in the reconstruction are fairly good, with a trend in underestimating slightly the values of

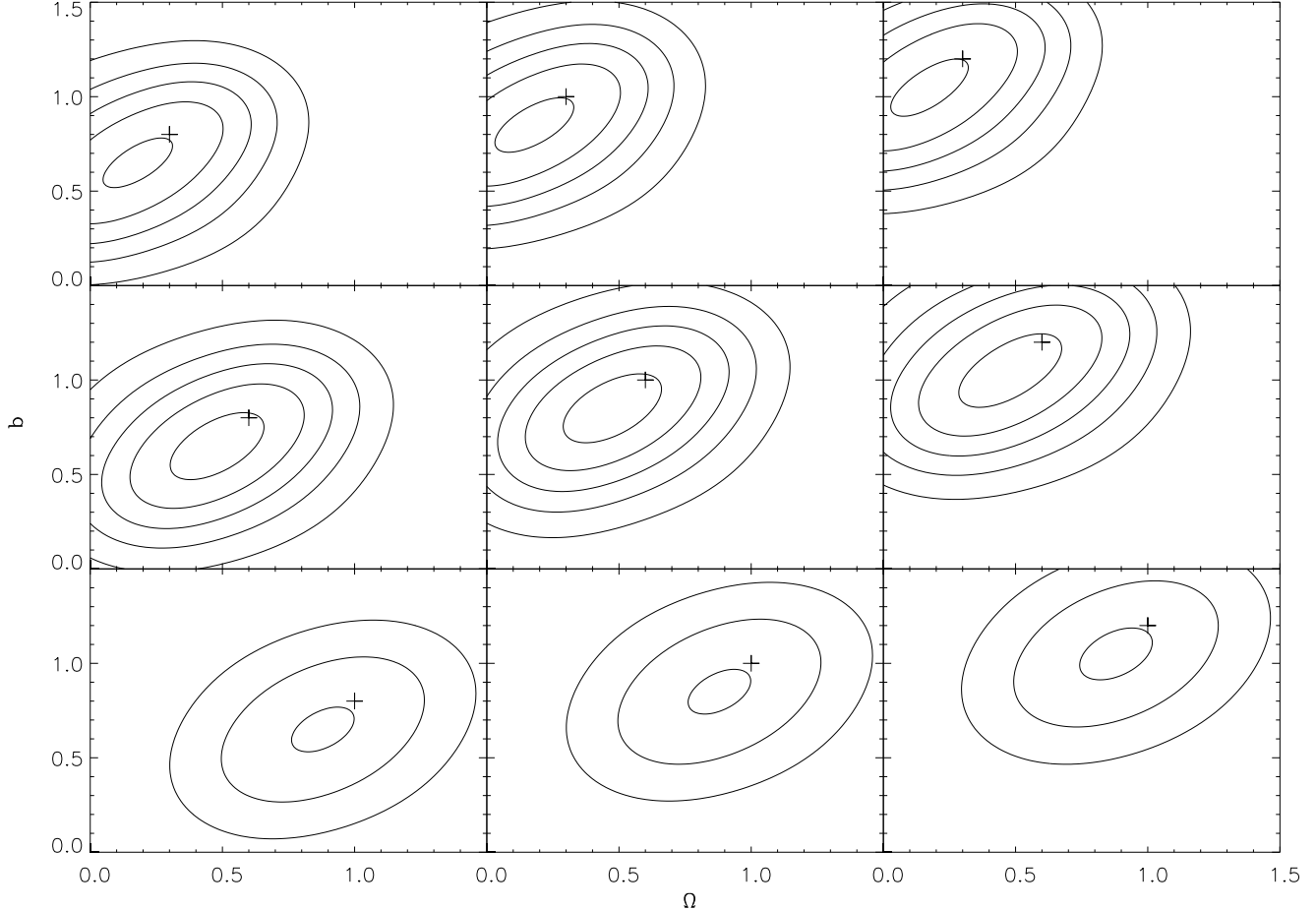


**Figure 2.** Likelihood contours for the reconstruction of the nine datasets  $d(b, \Omega_m)$ . The cross on each panel indicates the real values of  $(b, \Omega_m)$  in each reconstruction, and the likelihood contours are computed following (32) with a suitable normalization. The concentric contours represent a likelihood of 95%, 75%, 50%, 25% and 10% from the inner curves to the outer, on the two upper rows, and 95%, 75% and 50% on the lower row.

both parameters. The best reconstructions are for the intermediate value of the density parameter  $\Omega_m = 0.6$ , shown in the second row. In this case the crosses actually lie within the highest likelihood contours, with very little scatter. Overall, in the nine reconstructions the rms scatter in  $b$  and  $\Omega_m$  lie within the region  $0.26 \lesssim \sigma_b^2 \lesssim 0.44$ ,  $0.15 \lesssim \sigma_{\Omega_m}^2 \lesssim 0.32$ . The largest scatter in  $\Omega_m$  is for  $\Omega_m = 0.6$ , and a similar situation arises with  $b$ , whereby the intermediate value  $b = 1.0$  has the larger error.

The effect of underestimating the true values of the parameters is systematic and can be calibrated. This effect can be largely ascribed to the unconventional choice of likelihood estimator (32). One could argue that, for slowly varying variances,  $\lambda \propto b^{-2}$  (chiefly from the  $\delta$  part of the RHS of (32)) and therefore smaller values of the bias factor (and consequently, by correlation, also of  $\Omega_m$ ) are favoured. However, it is not straightforward to disentangle the dependence of the solutions on the parameters after successive iterations. The likelihood estimator used is thus to some extent biased. However, we find that the criterion of convergence given by the RHS of (32), suitably normalised, is the sharpest discriminator to pin down the best estimates of the cosmological parameters. We have carried out numerous tests with

more conventional likelihood estimators (e.g. Fisher likelihood matrix, etc) obtaining much poorer results than with (32).

Fig. 3 shows the density contrast reconstructions for the same datasets  $d(b, \Omega_m)$ . The reconstructed density contrast  $\delta_{\text{LAP}}$  is shown on the horizontal axis plotted point-by-point within the selected spherical volume ( $r \sim 13,000 \text{ km s}^{-1}$ ) against the real density contrast of the mock datasets. A solid line of slope 1.0 is plotted across each panel that does not correspond to the regression line on each panel though the differences are tiny. The slopes of the regression lines lie within the range  $0.99 \pm 0.08$ . The rms value corresponding to the random and numerical errors lies in the range  $0.19 \lesssim \sigma_{\delta} \lesssim 0.28$ . The reconstructions in Fig. 3 have been carried out with a prior knowledge of the values of  $b, \Omega_m$  for each dataset. Alternatively, the test can be carried out by putting together the procedure followed to obtain the likelihood in Fig. 2 and investigate the scatter resulting in the plots  $\delta_{\text{mock}}$  vs.  $\delta_{\text{LAP}}$  for different values of  $b, \Omega_m$ . Supposedly estimating the values of  $b, \Omega_m$  and finding the optimal correlation between  $\delta_{\text{mock}}, \delta_{\text{LAP}}$  ought to be two not unrelated operations. However these two appear to be fairly independent: it turns out that whereas (32) gives us the correct

likelihood estimates following the criterion of convergence of the solutions at each iteration, the variations in  $\sigma_\delta$  for a large range of  $b, \Omega_m$  are fairly small, and  $\sigma_\delta$  (as computed from tests such as the nine reconstructions in Fig. 3) is too insensitive to be helpful in the estimate of the parameters. Therefore the tests show that the estimate of the parameters and the reconstruction of the fields are two operations that are to a large extent independent. For an arbitrary sample, one would thus first compute (32), pick the values of  $b, \Omega_m$  at the maximum of the likelihood surface and use these to solve the equations to compute  $\delta, \alpha$ . Similarly, Fig. 4 shows the comparison of the LAP results with the mock data in the reconstruction of the velocity potential. The values of the fields have been scaled to  $\alpha_{\max}$  and are dimensionless. It is apparent that the regression line is in all cases slightly greater than unity, with a more accentuated tilt for larger values of  $(b, \Omega_m)$ . The smaller values of  $\alpha$  adjust better to a slope of unity, but with larger scatter than larger  $\alpha$ .

Fig. 5 shows a cross-section on the  $Z = 0$  plane of a particular velocity field reconstruction, that of the dataset  $d(b = 1.0, \Omega_m = 0.3)$ . The figure shows several prominent features of the underlying density field in this case: three overdense regions to which the field vectors converge, on the lower left, middle right and upper left parts of the panel, and two prominent underdense regions, from which the velocities diverge, one at the central region and another one at the middle-left boundary of the circle. It is apparent that the LAP velocities are not vanishing in the normal direction of the boundary surface of the selected subvolume, and therefore the customary Neumann spatial boundary conditions employed on spherical Bessel functions (i.e. vanishing normal velocities at the boundary) do not apply. We note that spatial boundary conditions are unnecessary in the LAP reconstruction, thus we have not brought up the issue in §2. The velocity field agrees within 10% accuracy with the *n*-body exact field within 78% of the selected volume, and the remaining 22% differs from the mock sample velocities by an error of  $\gtrsim 10\%$  (shown in Fig. 4 by the regions enclosed by the solid curves) and within this volume 6% differs by an error  $\gtrsim 20\%$  (regions enclosed by broken curves). These regions are mostly located in the neighbourhood of peaks, right at the very slopes, where the largest velocities are found. The central regions of peaks and troughs are very accurately reconstructed, and it is indeed the intermediate regions that yield  $\delta$  points with greater scatter in Fig. 3 and worse velocity reconstructions in Fig. 5.

#### 4 BIAS AND $\Omega_m$ FROM IRAS 1.2 Jy

We apply the LAP method to the *IRAS* 1.2 Jy sample (Strauss *et al.* 1990, 1992; Fisher *et al.* 1995a) in the same way as we have used it in the reconstruction of the mock catalogs in §3. *IRAS* 1.2 Jy is not the largest existing near all-sky galaxy redshift catalogue, and it is now superseded by PSCz (Canavezes *et al.* 1998) which contains  $\sim 15,000$  galaxies, so this application is simply an illustration on how the LAP method can be used to break the degeneracy in the estimates of  $b$  and  $\Omega_m$ . Other large redshift samples of partial coverage can also be looked at with the LAP method, e.g., Las Campanas and the forthcoming Anglo-Australian 2dF ( $\sim 250,000$  galaxies) and US Sloan Digital Sky Survey

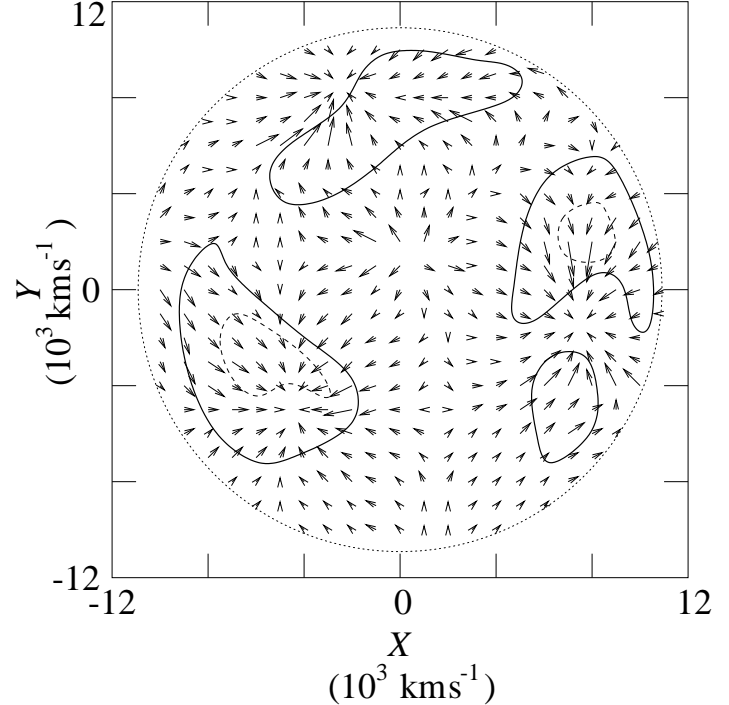


**Figure 5.**  $Z = 0$  plane reconstruction of the velocity field within a selected subvolume  $x_{\max} \lesssim 12,000 \text{ km s}^{-1}$  for the mock sample  $d(b = 1.0, \Omega_m = 0.3)$ . The solid lines enclose regions where the reconstruction entails an error  $|\vec{v}_{\text{mock}} - \vec{v}_{\text{LAP}}|/v_{\text{mock}} \gtrsim 0.10$  and within the broken lines this error is  $\gtrsim 0.20$ .

(SDSS) ( $\sim 10^6$  galaxies and 25% coverage), with the caveat that boundary regions will be a source of propagating errors in the dynamical evolution. Even so, a large number of galaxies in a redshift survey of limited coverage can provide a good representation of the underlying density field, almost definitely outweighing the disadvantages of sampling a partial region of the sky, and it will be thus predictably worthwhile to apply the LAP method to those surveys. The *IRAS* 1.2 Jy sample contains 5320 galaxies distributed over 87.6% of the projected celestial sphere. The remaining unsampled 2.4% is an approximately disk-shaped region at a galactic latitude  $|b| \lesssim 5^\circ$ .

We adopt a Gaussian smoothing length of  $1200 \text{ km s}^{-1}$ , and make no assumption regarding the power spectrum. The data  $d_{\text{IRAS}}$  are distributed within a spherical region of radius  $x_{\max} \sim 15,000 \text{ km s}^{-1}$ . We use the dataset in a similar fashion as the mock samples  $d(b, \Omega_m)$  in the previous section to derive the  $x$ -space fields  $\delta, \alpha$ . In §3 we have established that  $\sigma_\delta, \sigma_\alpha$  are fairly insensitive to the values of  $b, \Omega_m$ . One can thus set out to investigate the likelihood function  $\lambda(b, \Omega_m)$  as defined in (32) prior to determining the reconstructed fields. Evidently this is the simplest way to proceed for, unlike in §3, we do not have any clue about the real-space underlying fields (such as  $\delta_{\text{mock}}, \alpha_{\text{mock}}$  in §3) to compare them with the reconstructed fields.

The likelihood contour plot is shown in Fig. 6. Clearly the largest values of the likelihood function are centered around  $b \sim 1$  and small  $\Omega_m$ . From the test of the LAP method in §3 with *n*-body simulations we already know that the likelihood function (32) underestimates both  $b$  and  $\Omega_m$ , as is apparent in all nine panels of Fig. 2. We accept this

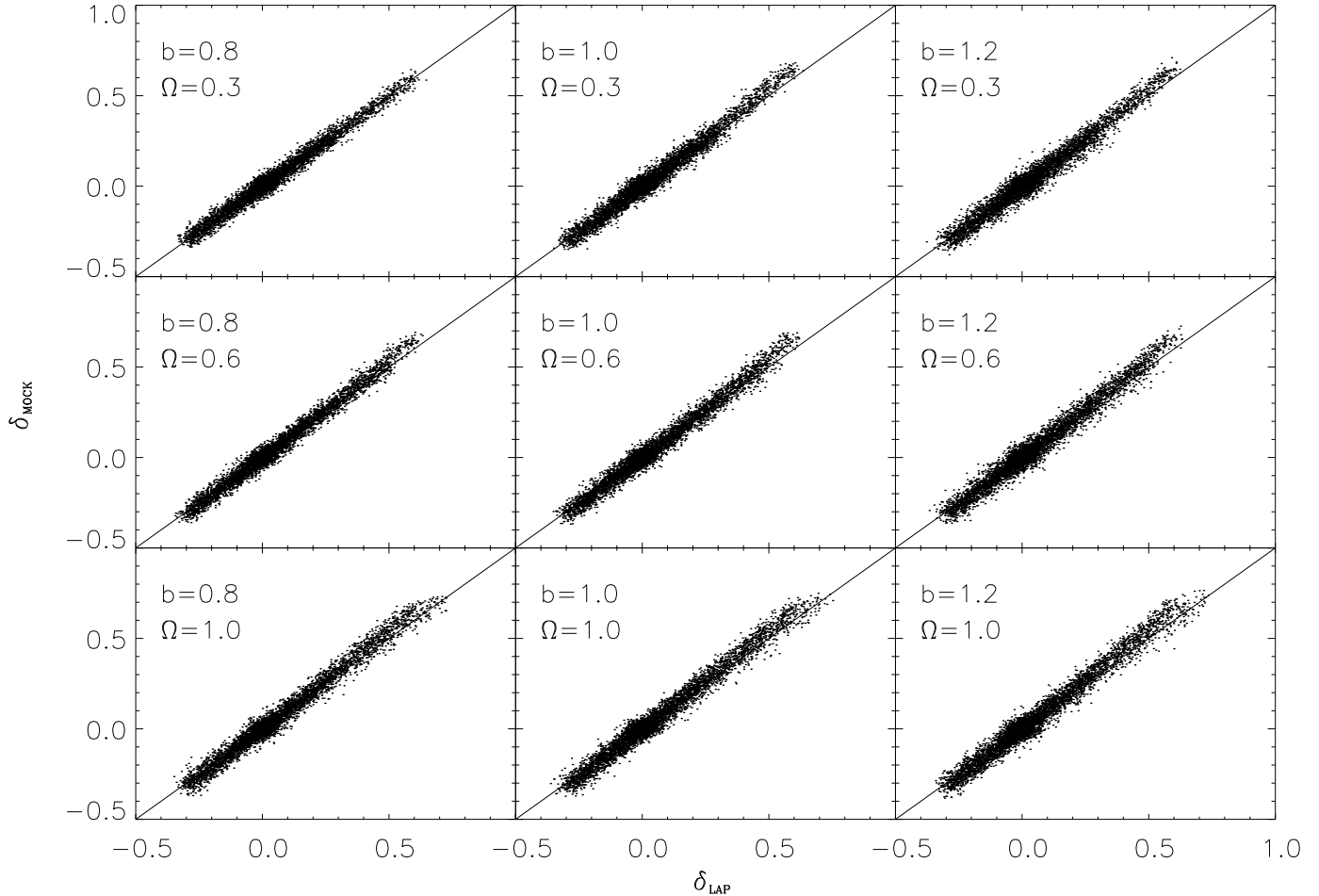


**Figure 3.** Density field reconstructions of the nine datasets  $d(b, \Omega_m)$ . The smoothed density contrast of the mock samples (vertical axis) is compared at each point within a selected spherical volume of the  $128^3$  grid with the LAP-reconstructed densities (horizontal axis) over a sphere of radius  $\sim 13,000 \text{ km s}^{-1}$ . The systematic errors are caused by the sparseness of the sampling.

trend is fairly inherent to the numerical application of the method and thus infer that the result presented in Fig. 6 is no different in this respect, and therefore the *real* values of the parameters are situated somewhat above their maxima in the likelihood function. From Fig. 2 one can quantify these errors to be of the order of  $\Delta\Omega_m \approx 0.12$ ,  $\Delta b \approx 0.15$ . Therefore, we infer that in Fig. 6 the likelihood maxima and the real values of the parameters are likely to be offset by a similar margin of error. At face value, Fig. 6 estimates that the most likely values of the parameters are  $\Omega_m \approx 0.18$  and  $b \approx 0.94$ . If we offset these estimates by the errors derived from Fig. 2, then the likely “real” values of the parameters that we obtain for Fig. 6 are  $\Omega_m \approx 0.31$  and  $b \approx 1.1$ . As a matter of fact, these offset values are still within the region enclosed by the 95% confidence contour.

To put our results in perspective with previous analyses of *IRAS* 1.2 Jy, we have overlaid on the contour plot of Fig. 6 two previous estimates of  $\beta \equiv \Omega_m^{0.6}/b$ . An estimate by Willick *et al.* (1997a) yields  $\beta_I = 0.49 \pm 0.07$  (shaded region *A*) and an estimate by Sigad *et al.* (1998) yields  $\beta_I = 0.89 \pm 0.12$  (shaded region *B*). The estimate of Willick *et al.* (1997a) is clearly in better agreement with our results as the location of the offset maximum of the likelihood is contained within the shaded region *A* that corresponds to the error margin

of their estimate. The estimate given by shaded region *B* is consistent with a scenario  $b \approx 1$ ,  $\Omega_m \approx 1$ , which in our analysis falls well outside the 10% likelihood contour.

Fig. 7 shows a  $z$ -space comparison between the reconstructed fields and the dataset. The data on the horizontal axis,  $\delta_{\text{LAP}}^s$ , is obtained from the reconstructed  $x$ -space fields  $\delta, \alpha$  via (11). The combination of both fields via the relationship  $\delta_{\text{LAP}}(\vec{x}) \propto \delta_s(\vec{x} + \hat{x}\alpha'_{\text{LAP}})$  permits us to reconstruct  $\delta_s$  which is our only possible point of comparison with  $\delta_{\text{IRAS}}$ , and this is shown in Fig. 7. The vertical axis shows the  $z$ -space data points of the smoothed *IRAS* 1.2 Jy sample. The data are plotted in a point-by-point comparison for all the grid points within the selected subvolume. A solid line of slope 1.0 is plotted across the diagonal of the plot. The slope of the regression line is slightly over the diagonal line, at approximately 1.03. The corresponding rms due to random and numerical errors in the LAP reconstruction is  $\sigma \approx 0.27$ . The values of the parameters that have been used in the reconstruction are  $b = 1.0$ ,  $\Omega_m = 0.3$ .

#### 4.1 Velocity fields

The resulting velocity field for the parameters of Fig. 7 is shown in Fig. 8. The six panels show the reconstructed

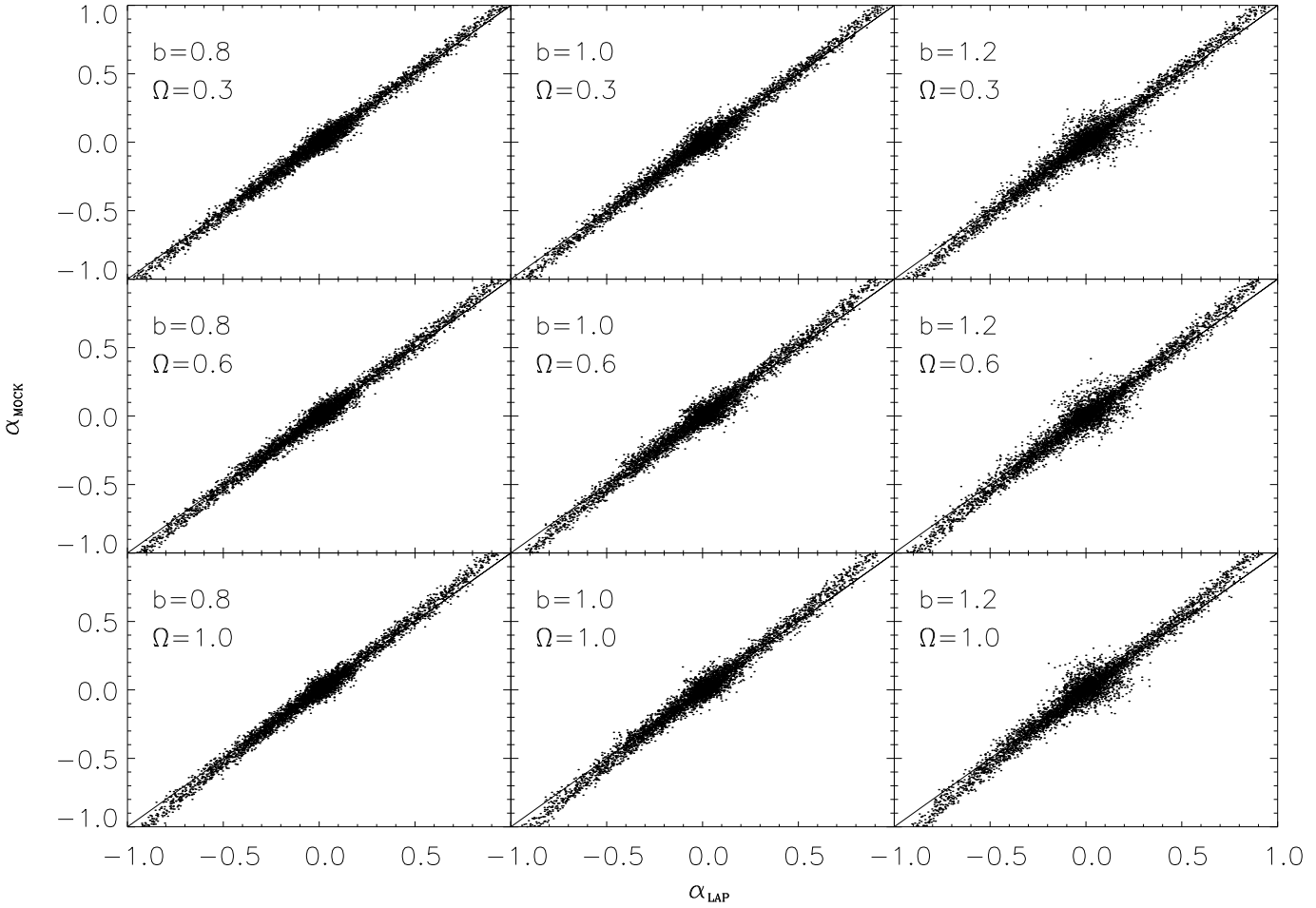


**Figure 4.** Velocity potential field reconstructions of nine datasets  $d(b, \Omega_m)$ . The velocity potential values are scaled to  $\alpha_{\max}$ , so that they are dimensionless and consigned to the range  $-1.0 \lesssim \alpha \lesssim 1.0$ . The smoothed velocity potential of the mock samples (vertical axis) is compared at each point within the same selected volume as in Fig. 3.

*IRAS* 1.2 Jy fields  $\delta_{\text{LAP}}$  and  $\vec{v}_{\text{LAP}}$  in supergalactic coordinates, for three different slices  $Z = 0, \pm 2000 \text{ km s}^{-1}$ . The velocity panels on the right column correspond to the densities on the left, at the same value of  $Z$ . The velocity field follows the main features observed on the  $\delta_{\text{LAP}}$  field, with a general flow towards the overdense regions and outflow from voids. The largest velocities are located in the intervening regions between overdense and underdense regions, e.g. in  $Z = 0$  (middle panels), large infall velocities are visible in the vicinity of the Comma supercluster (0,80,0), the Hydra-Centaurus (H-C) supercluster (-30,15,0), and Perseus-Pisces (P-P) (50,-5,0). In  $Z = 0$  the largest velocities are located at the lower right region of the H-C overdensity maximum, and also to the left of the P-P maximum. There is a velocity flow from the main void on the lower left of the figure, in the direction of Virgo, and it splits up to left and right, in manner of a ridge, to create an outflow in opposite directions, towards H-C and P-P. In the case of  $Z = -2000 \text{ km s}^{-1}$  (lower row), large velocities are also present around the steeper regions of the prominent overdensities, following a similar pattern as in  $Z = 0$ , whereas the field shows more erratic features in  $Z = 2000 \text{ km s}^{-1}$  (upper row), where the outflow from the main void (centre left) shows a general

trend towards the main overdense features but is at the same time prone to local variations.

The results presented in Figs. 6–8, can be optimized by using the Mark III velocity redshift survey to pin down  $b, \Omega_m$  more accurately. We shall pursue this and look for the optimal values of  $b, \Omega_m$  by computing the LAP solutions that satisfy

$$\delta \sum (\vec{v}_{\text{LAP}} - \vec{v}_{\text{MarkIII}})^2 = 0, \quad (33)$$

where  $\delta$  denotes a variation, not the density contrast. In practice, this is achieved as follows. One adds (33) to the two already existing constraints of the LAP method (18), (19). Those are tackled in the manner summarized in §2.5. In actual terms, it's far more practical to deal with (33) in terms of the velocity potential, so what we have done in the present analysis is in reality to compute  $\alpha_{\text{MarkIII}}$  from the smoothed observed velocity field, and thus used (33) in the manner of a second constraint on  $\alpha$ .

The comparison with the  $\vec{v}_{\text{MarkIII}}$  data sets further constraints on the likelihood contours of Fig. 6 as is shown below. Mark III contains approximately 3,400 galaxies, which are compiled from several sets of elliptical and SO galaxies (Willlick *et al.* 1995, 1996, 1997a). The sample spans out

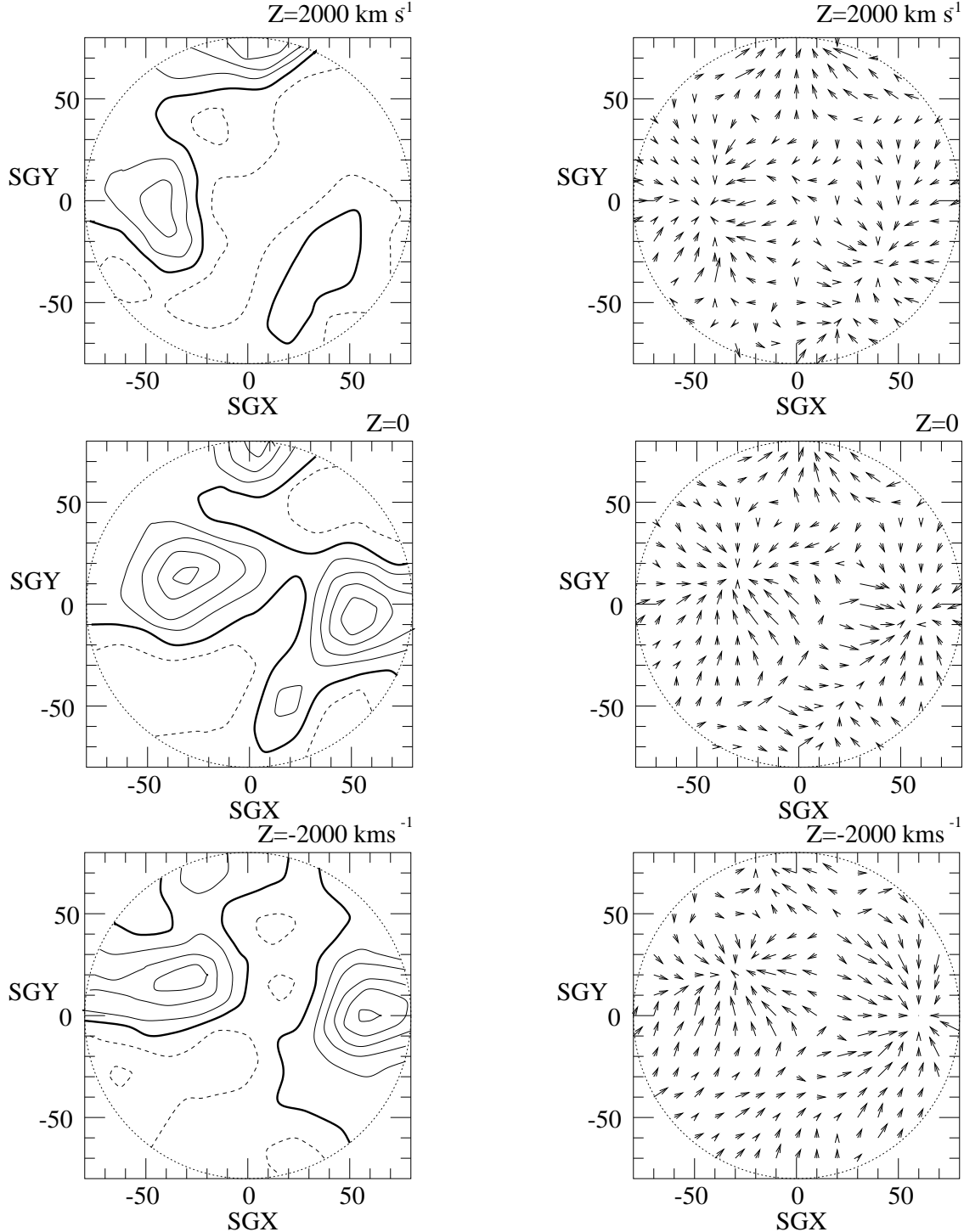


**Figure 8.**  $\delta_{\text{LAP}}$  and  $\vec{v}_{\text{LAP}}$  fields for IRAS 1.2 Jy. SGX and SGY units are in  $100 \text{ km s}^{-1}$ , spanning over a sphere of radius  $\sim 8000 \text{ km s}^{-1}$ . *Left:* from top to bottom panels, density contrast for a Gaussian smoothing of  $1200 \text{ km s}^{-1}$ , for  $Z = 2000, 0, -2000 \text{ km s}^{-1}$ . Thick solid line corresponds to  $\delta = 0$ , continuous contours are  $\delta > 0$  and slashed contours are  $\delta < 0$ ; contour spacing is 0.2. *Right:* from top to bottom, reconstructed velocities at same values of  $Z$ .

to  $\sim 6000 \text{ km s}^{-1}$ , though in some directions it is irregularly sampled to  $x_{\text{max}} \sim 8000 \text{ km s}^{-1}$  and  $x_{\text{min}} \sim 4000 \text{ km s}^{-1}$ . The distances are inferred via forward Tully-Fisher and  $D_n - \sigma$  distance indicators which may entail an error in the region 17–21%. Mark III predicts a bulk flow

$v_B \sim 194 \pm 32 \text{ km s}^{-1}$  towards the Shapley concentration (Zaroubi, Hoffman & Dekel 1999) (for a low-resolution Gaussian smoothing  $\sim 1200 \text{ km s}^{-1}$ , within a sphere  $r \sim 6000 \text{ km s}^{-1}$ ), in contrast to  $v_B \sim 250 - 400 \text{ km s}^{-1}$  that is estimated in most other samples, including PSCz (a compilation

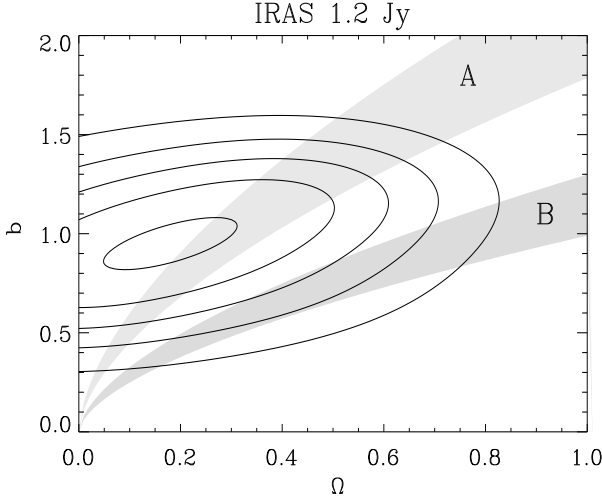


**Figure 6.** Likelihood contours for *IRAS* 1.2 Jy. The concentric contours represent a likelihood of 95%, 75 %, 50%, 25 %, 10% from the inner curve to the outer. The shaded region *A* corresponds to the estimate of  $\beta$  by Willick *et al.* (1997a) and the shaded region *B* corresponds to an estimate of  $\beta$  by Sigad. *et al.* (1998).

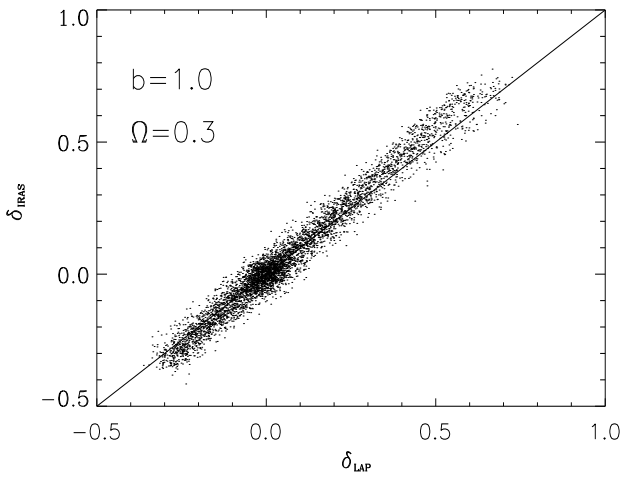


**Figure 7.** Redshift-space density contrast in the LAP reconstruction versus the corresponding *IRAS* 1.2 Jy data for a Gaussian smoothing of  $1200 \text{ km s}^{-1}$  within a spherical region of radius  $x_{\text{max}} \sim 15,000 \text{ km s}^{-1}$ . The field  $\delta_{\text{LAP}}$  is evaluated at  $b = 1.0$ ,  $\Omega_m = 0.3$ .

of  $v_B$  estimates is summarized in Dekel 1999b).  $\delta_{\text{IRAS}}$  and  $\delta_{\text{MarkIII}}$  are consistent with mildly non-linear gravitational instability and linear bias (Sigad *et al.* 1998), though there are some differences, e.g. the Mark III sample appears to show a strong shear across the Hydra-Centaurus complex that is absent in *IRAS* 1.2 Jy (as indeed also in ORS). Recent papers have studied in detail the differences between the *IRAS* 1.2 Jy and Mark III velocity and density fields (Sigad *et al.* 1998; also Dekel *et al.* 1999 following an improved version of POTENT).

We consider the Mark III sample with a Gaussian smoothing length of  $1200 \text{ km s}^{-1}$ . The data are carefully

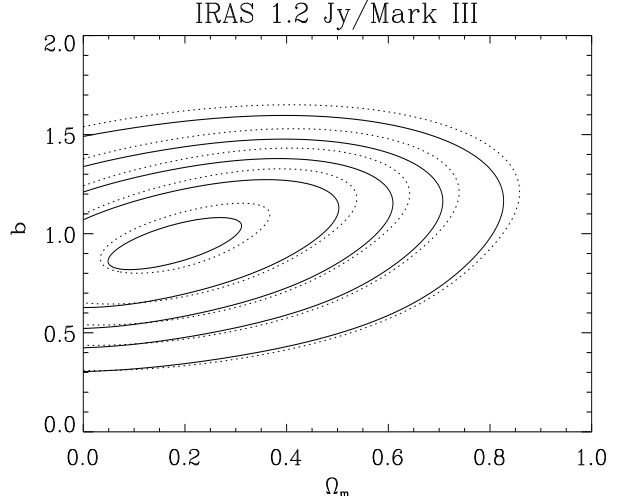


**Figure 9.** Solid contours represent the likelihood for *IRAS* 1.2 Jy as in Fig. 6, and dotted contours represent the likelihood in the *IRAS* 1.2 Jy/Mark III comparison following (33). The relative likelihood of the concentric contours is as in Fig. 6 in both solid and dotted.

corrected for Malmquist biases (following the recipe set out in Sigad *et al.* (1998) for the preparation of the data), and the distances of 1,241 objects are modified as a result. The LAP method is solved for *IRAS* 1.2 Jy within spherical volume of radius  $x_{\text{max}} \sim 15,000 \text{ km s}^{-1}$ , and the minimization fit with Mark III (33) is done within a spherical subvolume of radius  $\langle x \rangle \sim 6000 \text{ km s}^{-1}$ . Therefore most of the volume of the LAP solutions remains free of the constraint (33) and the fraction of the volume where  $\vec{v}_{\text{LAP}}$  is least-squared to  $\vec{v}_{\text{MarkIII}}$  is only 0.064. Naturally such a small fraction forecasts an almost negligible impact in the fine-tuning of the parameters, unless the fields differed drastically to start with, which they do not. The  $\vec{v}_{\text{LAP}}$  solution in the remainder of the volume is indirectly affected by this fit, and the variations in modulus  $\Delta v_{\text{LAP}}$  outside the comparison subvolume are  $\lesssim 12\%$ .

Fig. 9 shows the likelihood contours for  $(b, \Omega_m)$  computed via the adjustment entailed in (33). The solid contours are the purely *IRAS* 1.2 Jy prediction, as in Fig. 6, and the dotted contours are the result of the comparison with Mark III. The contours are ever so slightly shifted towards greater values of the parameters and, as expected, the effect is small. The shift towards larger  $b, \Omega_m$  is not in fact an altogether undesirable modification, as we have already discussed that the LAP solutions are found to be per se offset to smaller values than their “real” values. The important conclusion to be drawn from Fig. 9 is that the comparison with Mark III is entirely consistent with the predictions for  $b$  and  $\Omega_m$  extracted from the *IRAS* 1.2 Jy sample alone.

## 5 CONCLUSIONS

The LAP method provides a practical means to break the degeneracy between  $\Omega_m$  and  $b$  in galaxy redshift surveys. The method is employed in the manner of a nonlinear constraint on the redshift-space dataset and, although in for-

mulation it comes across as algebraically cumbersome, it is of considerable simplicity and efficiency from the numerical point of view. The method is sound in that it does not require an a priori approximation of the map  $\vec{x} \rightarrow \vec{s}$  to pin down the solution and it provides considerable freedom to ascribe relative importance to the data available, i.e. the initial and final endpoints, to which we wish to invariably assign greater weight than intermediate stages of which little or no data are available.

The method can prove significant to measure  $\Omega_m$  in the latest largest samples, and extract the most accurate information prior to comparison with other datasets, such as the CMB radiation power spectrum and SN data. One important challenge for the future is to attain a better grasp of the concept of bias and this will be probably achieved via microlensing data and  $n$ -body simulations of the formation of galaxies and clusters from primordial fluctuations, rather than from galaxy redshift surveys. Once a model of bias is adopted on a sound footing, then clearly the LAP model is impeccable in producing an estimate of  $\Omega_m$ . In the simple linear bias model we have employed we have totally relegated any consideration of scale-dependence in  $b$ . This is a point I have deliberately omitted for simplicity. Thus, the estimates computed in this paper ought to be regarded qualitatively as weighted averages of the ‘‘real’’  $b$  over different scales, if indeed scale-dependent bias models are to be believed.

In this paper, we have employed the likelihood function (32) to investigate the values of  $b, \Omega_m$ . Clearly this is not a unique choice. However, our choice is guided by the argument of relative convergence of the solutions, which is justifiably a reasonable criterion to get close to the ‘‘real’’ solutions. In view of the performance of the  $\lambda$  function in the reconstruction of the mock samples, this choice does not appear to be totally off the mark. A potential reason for concern could be the offset observed between the maxima of the likelihood functions and the real values of the parameters in the  $n$ -body simulations. However the recurrence of this offset in a predictable manner lends strength to the argument that it arises as a numerical fault that is easy to account for systematically in the analysis of the datasets. The reconstructions of the fields are, on the other hand, of considerable accuracy and no numerical deficiency or hindrance is observed. The application of the method to *IRAS* 1.2 Jy predicts the parameters to be fairly accurately located in the immediate neighbourhood of the maxima  $\Omega_m \approx 0.3$  and  $b \approx 1.1$ , which is found to be most compatible with the estimate of  $\beta$  given by Willick *et al.* (1997a). In a flat universe such predicted values are perfectly consistent with a non-vanishing cosmological constant or a quintessence scalar field component. The likelihood examined in this way is only very slightly modified when the velocities predicted via the LAP method are finely-tuned with data from the Mark III sample. The shift of the predicted values is towards slightly greater values of the parameters but it remains comfortably consistent with the results obtained from *IRAS* 1.2 Jy.

## ACKNOWLEDGMENTS

The numerical analysis has been performed in the *Starlink* facilities at Queen Mary & Westfield College (London), and thanks are due to a number of people for supplying

and lending a helping hand with technicalities regarding the data. The author thanks an anonymous referee for insightful comments that have greatly improved the readability of the manuscript. This research has been funded in part at EHU by research grant UPV172.310-G02/99.

## REFERENCES

Abramowitz M., Stegun I.A., 1972, *Handbook of Mathematical Functions*, Dover, New York

Baker, J.E., Davis M., Strauss M.A., Lahav O., Santiago B.X., 1998, ApJ 508, 6

Bernardeau F., Juszkiewicz R., Dekel A., Bouchet F., 1995, MNRAS 274, 20

Branchini E., Carlberg R.G., 1994, ApJ 434, 37

Canavezes A. *et al.*, 1998, MNRAS 297, 777

Coles P., Sahni V., 1995, Phys. Rep. 262, 1

Courant R. and Hilbert D., 1989, *Methods of Mathematical Physics*, John Wiley & Sons, New York, vol. I

Dekel A., 1994, Annu. Rev. Astron. Astrophys., 32, 371–418

Dekel A., 1999a, in *Formation of Structure in the Universe*, ed. A. Dekel and J.P. Ostriker, Cambridge University Press, 250

Dekel A., 1999b, in *Cosmic Flows: Towards an Understanding of Large-Scale Structure*, eds. S. Courteau, M.A. Strauss and J.A. Willick, ASP Conf. Series

Dekel A., Lahav O., 1999, ApJ 520, 24

Dekel A., Bertschinger E., Yahil A., Strauss M.A., Davis M., Huchra J.P., 1993, ApJ 412, 1

Dekel A., Burstein D., White S.D.M., 1997, in *Critical Dialogues in Cosmology*, ed. N.G. Turok, World Scientific, Singapore

Dekel A., Eldar A., Kolatt T., Yahil A., Willick J.A., Faber S.M., Courteau S., Burstein D., 1999, ApJ 522, 1

Fisher K.B., Davis M., Strauss M.A., Yahil A., Huchra J.P., 1993, ApJ 402, 42

Fisher K.B., Huchra J.P., Strauss M.A., Davis M., Yahil A., Schlegel D., 1995a, ApJS 100, 69

Fisher K.B., Lahav O., Hoffman Y., Lynden-Bell D., Zaroubi S., 1995b, MNRAS 272, 885

Fry J.N., 1994, Phys. Rev. Lett. 73, 2

Giavalisco M., Mancinelli B., Mancinelli P.J., Yahil A., 1993, ApJ 411, 9

Hudson M.J., Dekel A., Courteau S., Faber S.M., Willick J.A., 1995, MNRAS 274, 305

Kaiser N., 1987, MNRAS 227, 1

Linde A., Sasaki M., Tanaka T., 1999, Phys. Rev. D59, 123522

Peebles P.J.E., 1989, ApJ 344, L53

Peebles P.J.E., 1990, ApJ 362, 1

Santiago B.X., Strauss M.A., Lahav O., Davis M., Dressler A., Huchra J.P., 1995, ApJ 446, 457

Saunders W., Sutherland W., Maddox S., Keeble O., Oliver S.J., Rowan-Robinson M., Mahon R.G., Efstathiou G.P., Tadros H., White S.D.M., Frenk C.S., Carramiñana A., Hawkins M.R.S., 2000, MNRAS submitted, astro-ph/0001117

Schmidt I.M., Saha P., 1999, AJ 115, 2231

Shaya E.J., Peebles P.J.E., Tully R.B., 1995, ApJ 454, 15

Sigad Y., Eldar A., Dekel A., Strauss M.A., Yahil A., 1998, ApJ 495, 516

Strauss M.A., Davis M., Yahil A. and Huchra J.P., 1990, ApJ 361, 49; general descriptive information on *IRAS* 1.2 Jy can be found in <http://www.gsfc.nasa.gov/astro/iras/irs.html>

Strauss M.A., Huchra J.P., Davis M., Yahil A., Fisher K.B., Tonry J., 1992, ApJS 83, 29

Strauss M.A., Willick J., 1995, Phys. Rep. 261, 271

Susperregi M., 1995, D.Phil. thesis (Oxford), unpublished

Susperregi M., 2000, in proc. 4th RESCEU symposium on *The*

*Birth and Evolution of The Universe*, Tokyo, World Scientific, in press

Susperregi M., Binney J., 1994, MNRAS 271, 719 (SB94)

Tadros H., Ballinger W.E., Taylor A.N., Heavens A.F., Efstathiou G., Saunders W., Frenk C.S., Keeble O., McMahon R., Maddox S.J., Oliver S., Rowan-Robinson M., Sutherland W.J., White S.D.M., 1999, MNRAS 305, 527

Verde L., Heavens A.F., Matarrese S., Moscardini L., 1998, MNRAS 300, 747

Willick J.A., Courteau S., Faber S.M., Burstein D., Dekel A., Kollat T., 1995, Ap. J. 446, 12 (paper I)

Willick J.A., Courteau S., Faber S.M., Burstein D., Dekel A., Strauss M.A., Kollat T., 1996, Ap. J. 457, 460 (paper II)

Willick J.A., Courteau S., Faber S.M., Burstein D., Dekel A., Strauss M.A., 1997a, ApJS 109, 333 (paper III)

Willick J.A., Strauss M.A., Dekel A., Kollat T., 1997b, ApJ 486, 629

Yahil A., Strauss M.A., Davis M., Huchra J.P., 1991, ApJ 372, 380

Zaroubi S., Hoffman Y., Dekel A., 1999, ApJ 520, 413

## APPENDIX A: ORBIT-CROSSING IN REDSHIFT SPACE

We shall prove the boundary condition (11). The number-counts of galaxies  $n$  in  $x$ -space and  $z$ -space satisfy, by conservation of the number of galaxies:

$$dn(\vec{s}) = \sum_{\text{streams}} dn(\vec{x}_i), \quad (\text{A1})$$

for all streams at the same redshift,  $\vec{s} = \vec{x}_i + \hat{x}(\hat{x} \cdot \nabla_x \alpha_i)$ . In our analysis we shall only consider single-valued solutions, and therefore there is just one stream only in (A1), i.e.  $dn(\vec{s}) = dn(\vec{x})$ . Hence

$$\rho_s(\vec{s}) d\Omega \equiv \frac{dn(\vec{s})}{ds} = x^2(1+b\delta) \frac{N_{\text{gals}}}{V} \frac{dx}{ds} d\Omega, \quad (\text{A2})$$

where  $n(\vec{s})$  is the galaxy number-count,  $d\Omega$  a solid angle element and the  $x$ -space selected volume of the sample is  $V \sim \frac{4}{3}\pi x_{\text{max}}^3$ , and

$$s \equiv \hat{x} \cdot \vec{s} = x + \alpha'. \quad (\text{A3})$$

Therefore

$$\frac{dx}{ds} = \frac{1}{1 + \alpha''}, \quad (\text{A4})$$

and substituting this in (A2), we get

$$\rho_s = x^2 \frac{N_{\text{gals}}}{V} \left( \frac{1 + b\delta}{1 + \alpha''} \right). \quad (\text{A5})$$

In the case of multistreams, the RHS of (A5) is integrated over all streams, bearing in mind that *turn-around* regions, which occur at  $\delta \gg 1$  and for which  $ds/dx = 0$ , are excluded from the sum. An example of such a region is shown in Fig. A1. An initial saddle-point  $ds/dx = 0$  on the  $s(x)$  curve starts the creation of a turn-around region. At the stage shown in Fig. A1, both points  $A$  and  $B$  satisfy this condition and obviously they departed from an initial saddle-point  $A = B$ . The region spanning between  $A$  and  $B$  is three-valued (each redshift in the interval  $z_B < z < z_A$  corresponds to three  $x$  positions), whereas  $z_A$  and  $z_B$  are bivalued. To make such an scenario tractable, we need to replace  $s(x)$  over the interval  $z_B < z < z_A$  by a monotonic

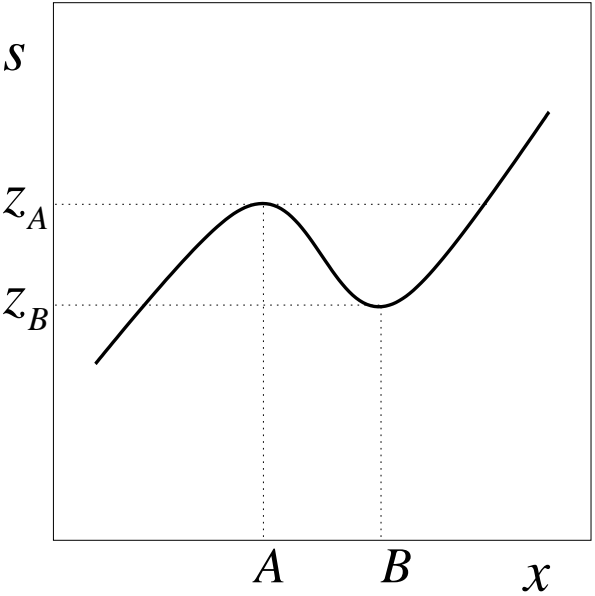


**Figure A1.** Illustration of a turn-around region.

curve that matches the existing curve at  $z_B$  and  $z_A$  and its first derivative. This is obviously tantamount to applying a larger smoothing length than the existing one to erase the overdense region that is the cause of the turn-around.

## APPENDIX B: EVALUATION OF RADIAL DERIVATIVES

The radial derivative of the velocity potential coefficients (15) can be written as

$$\frac{d}{dx} \alpha_n = \sum_{rlm} \alpha_{rlm}'^{(n)} j_l(k_r x) Y_{lm}, \quad (\text{B1})$$

where, using the equality

$$\frac{d}{du} j_l(u) = (2l+1)^{-1} \left[ l j_{l-1}(u) - (l+1) j_{l+1}(u) \right], \quad (\text{B2})$$

we have

$$\alpha_{rlm}'^{(n)} = k_r \left[ \frac{(l+1)}{(2l+3)} \alpha_{r(l+1)m}^{(n)} - \frac{l}{(2l-1)} \alpha_{r(l-1)m}^{(n)} \right]. \quad (\text{B3})$$

Similarly

$$\begin{aligned} \alpha_{rlm}''^{(n)} &= k_r^2 \left\{ \frac{(l+1)}{(2l+3)} \frac{(l+2)}{(2l+5)} \alpha_{r(l+2)m}^{(n)} \right. \\ &\quad \left. - \left[ \frac{(l+1)^2}{(2l+3)(2l+1)} + \frac{l^2}{(2l-1)(2l+1)} \right] \alpha_{rlm}^{(n)} \right. \\ &\quad \left. + \frac{l}{(2l-1)} \frac{(l-1)}{(2l-3)} \alpha_{r(l-2)m}^{(n)} \right\}. \end{aligned} \quad (\text{B4})$$

On the other hand, the coefficients  $\bar{J}_{lm}^{(n)}$  given in (16) are

$$\bar{J}_{lm}^{(n)} = \sum_r \left[ \frac{\alpha(l, m+1)}{2} \alpha_{rl(m+1)}^{(n)} (i\hat{x}_1 - \hat{x}_2) \right]$$

$$+ \frac{\beta(l, m-1)}{2} \alpha_{rl(m-1)}^{(n)} (i\hat{x}_1 + \hat{x}_2) + im \alpha_{rlm}^{(n)} \hat{x}_3 \Big], \quad (B5)$$

where

$$\alpha(l, m) = \left[ l(l+1) - m(m-1) \right]^{1/2}, \quad (B6)$$

$$\beta(l, m) = \left[ l(l+1) - m(m+1) \right]^{1/2}. \quad (B7)$$

## APPENDIX C: CHEBYSHEV POLYNOMIALS

The Chebyshev polynomials are defined  $T_n(\cos \theta) \equiv \cos(n\theta)$  (following the normalization of Abramowitz & Stegun 1972). We define the angle brackets  $\langle , \rangle$  according to the orthogonality properties of  $T_n$  (e.g. Courant & Hilbert 1989):

$$\langle u \rangle \equiv \int_{-1}^1 dt w(t) u(t), \quad (C1)$$

where  $w(t) = (1-t^2)^{-1/2}$  is a weight function and therefore

$$\langle T_n T_m \rangle = \delta_{nm} \frac{\pi}{2}, \quad (C2)$$

for  $n \neq 0$  and  $\langle T_0^2 \rangle = \pi$ . In (22)(23) we encounter two types of angle brackets to evaluate (other than (C2)):  $\langle T_n \dot{T}_m \rangle$  and  $\langle T_n T_m T_r \rangle$  (we have deliberately omitted  $\langle \Omega_m T_n T_m \rangle$ , by approximating  $\Omega_m$  by a constant, and ditto for  $H$ . The second type of product is trivially transformed into (C2) via

$$2T_n T_m = T_{n+m} + T_{n-m} \quad (C3)$$

for  $n \geq m$ , and the first requires a little numerical manipulation using the relation

$$(1-t^2) \dot{T}_n = -nt T_n + T_{n-1}. \quad (C4)$$

## APPENDIX D: ORTHOGONALITY RELATIONS

The orthogonality relations for the spherical harmonics and the Bessel functions are respectively

$$\int_0^{2\pi} d\varphi \int_0^\pi d(\cos \theta) Y_{lm} Y_{l'm'} = \delta_{ll'} \delta_{mm'}, \quad (D1)$$

$$\int_0^1 dx x^2 j_l(k_r x) j_l(k_s x) = \frac{1}{2k_r k_s} \left[ j_l(k_r x) + x j_l'(k_r x) \right]^2 \delta_{rs}. \quad (D2)$$

This paper has been produced using the Royal Astronomical Society/Blackwell Science L<sup>A</sup>T<sub>E</sub>X style file.